



Letter

Flexible infrared photodetector based on indium antimonide nanowire arrays

Muhammad Shafa^{1,2,5} , Di Wu^{1,5}, Xi Chen¹, Naveed ul Hassan Alvi³, Yi Pan¹  and Adel Najjar⁴

¹ Center for Spintronics and Quantum Systems, State Key Laboratory for Mechanical Behavior of Materials, Xi'an Jiaotong University, Xi'an, 710049, People's Republic of China

² XJTU-YLU Institute for Industrial Innovation of New Materials, Yulin University, Yulin 719000, People's Republic of China

³ RISE Research Institutes of Sweden, Bredgatan 33, PO Box 787, SE-601 17 Norrköping, Sweden

⁴ Department of Physics, College of Sciences, United Arab Emirates University, Al Ain, 15551, United Arab Emirates

E-mail: yi.pan@xjtu.edu.cn

Received 20 December 2020, revised 13 February 2021

Accepted for publication 24 February 2021

Published 14 April 2021



CrossMark

Abstract

Narrow bandgap semiconductors like indium antimonide (InSb) are very suitable for high-performance room temperature infrared photodetectors, but the fragile nature of the wafer materials hinders their application as flexible/wearable devices. Here, we present a method to fabricate a photodetector device of assembled crystalline InSb nanowire (NW) arrays on a flexible substrate that balances high performance and flexibility, facilitating its application in wearable devices. The InSb NWs were synthesized by means of a vapor–liquid–solid technique, with gold nanoclusters as seeding particles. The morphological and crystal properties were investigated using scanning electron microscopy, x-ray diffraction and high-resolution transmission electron microscopy, which revealed the unique spike shape and high crystallinity with (111) and (220) planes of InSb NWs. The flexible infrared photodetector devices were fabricated by transferring the NWs onto transparent and stretchable polydimethylsiloxane substrate with pre-deposited gold electrodes. Current versus time measurement of the photodetector devices under light showed photoresponsivity and sensitivity to mid-infrared at bias as low as 0.1 V while attached to curved surfaces (suitable for skin implants). A high-performance NW device yielded efficient rise and decay times down to 1 s and short time lag for infrared detection. Based on dark current, calculated specific detectivity of the flexible photodetector was 1.4×10^{12} Jones. The performance and durability render such devices promising for use as wearable infrared photodetectors.

Keywords: nanowires, infrared photodetector, flexible devices, indium antimonide (InSb)

(Some figures may appear in colour only in the online journal)

1. Introduction

Due to their high carrier mobility and relatively narrow bandgap, antimonide-based compound semiconductors have

been extensively investigated for applications in photosensors [1], gas sensors [2, 3], terahertz detectors, and high-frequency devices [4]. Being the member with the narrowest bandgap, indium antimonide (InSb) has some unique electronic and optoelectronic properties, i.e. a bandgap of 0.163 eV [5], electron mobility of $105 \text{ cm}^2 \text{ V}^{-1} \text{ s}^{-1}$ [6], and thermal

⁵ These authors have contributed equally to the work.

conductivity of $16.0 \text{ W m}^{-1} \text{ K}^{-1}$ [7]. InSb is very sensitive to light in the range of $1\text{--}5 \mu\text{m}$, and thus becomes an excellent material for infrared photodetectors [8]. In recent years, based on wafer-scale single crystal materials, and industrial semiconductor technology, InSb has found various applications, e.g. thermal imaging [9], temperature monitoring [10], and flame sensing [11].

On the other hand, the demand for flexible electronics devices has been quickly increasing due to the development of wearable gadgets with varying sensors [12] as these devices are sizeable, bendable, and readily utilized. Due to their ultralight weight, these wearable electronics have enormous potential as electronic skin [13], personal health care [14], and soft robotics [15]. However, most of the electronic devices fabricated on a semiconductor wafer are not flexible because of the stiff and fragile nature of such materials, including InSb. To tackle this problem, low-dimensional counterpart materials, like InSb nanowires (NWs), have attracted attention due to the advantages in flexibility when these are transferred to soft substrates. The flexibility originates from the movable contacts between the packed NWs, although the single NWs are crystalline and stiff. Additionally, the low-dimensional nature endows InSb NWs with some properties superior to bulk materials. The large surface-to-volume ratios could enhance photosensitivity due to increased surface defects sites for chemisorption of oxygen [16–18]. Low dimensionality of the interactive surface may boost the transportation speed inside the device [18]. Thus, compared with bulk materials or thin films, NWs show a higher sensitivity to light.

Growth of InSb NWs by an electrodeposition method was reported for the first time in 2005 [19], followed by the exploration of one-dimensional pure InSb and its heterojunctions. Since that time, it has remained a material of much interest to researchers. InSb NWs can be synthesized by different techniques, e.g. thermal chemical vapor deposition [20], physical vapor deposition [1, 21], electrodeposition in porous templates [22], metal-organic chemical vapor deposition [23], and molecular beam epitaxy [24]. To date, numerous growth techniques have been reported for the successful growth of InSb NWs. However, only a few of them have used an alumina furnace tube for the synthesis because it is still very challenging to grow InSb NWs with a diameter smaller than the Bohr radius. By using a Au catalyst layer this problem has been solved. Now, we can control the dimension of InSb NWs with the help of the seeding particle layer as well as the flow rate of the precursors. InSb NWs have been grown on Si substrate by using InSb powder via a vapor-liquid-solid (VLS) growth mechanism under an In-rich environment. For example, Ye *et al* [25] have deposited only In in order to make an In-rich surface of the substrate; however, in a conventional single zone tube furnace, it is still very challenging to control the ratio of III–V semiconductor materials. Among all growth techniques, VLS is a common growth mechanism that provides diameter controllability and high crystallinity. To date, capacitive and resistive techniques have been exploited to achieve wearable electronics detectors.

For example, polycarbonate membranes have been demonstrated as a template for InSb NWs [26].

Although the InSb wafer-based photodetector has been well studied, a flexible InSb photodetector that could be applied in wearable devices is still lacking. In this work, we report a method for the fabrication of a flexible mid-infrared photodetector by assembling an InSb NW array on polydimethylsiloxane (PDMS) substrates. Such devices have excellent photoresponsivity and sensitivity to xenon lamp and mid-infrared illumination with no time lag, and could be attached to arbitrarily curved surfaces, thus showing their potential application as wearable infrared photodetectors.

2. Experiment

The substrate for the InSb NWs is Si(111) wafer, which was coated with a 30–100 nm Au layer as a seeding particle using ion sputtering coating. To convert these seeding layers into nano-islands, substrates were subjected to annealing at elevated temperatures inside the furnace tube. These particles have low eutectic temperature, serving as the metal catalyst for the growth of low-dimensional materials using a VLS methodology. Growth dynamics of the one-dimensional material were investigated by changing the flow rate of the carrier gas, including other growth parameters like source and substrate temperature, and vacuum. Some of the NWs grown were quantum wires, as their radius was less than the Bohr radius of 60 nm [27]. Herein a facile route was adopted to fabricate the device from grown NWs which exhibit photodetection.

The vapor pressure of In and Sb precursors were at 1:1 while the growth temperature was $800 \text{ }^\circ\text{C}$ and $700 \text{ }^\circ\text{C}$, respectively. The substrates were placed downstream of the furnace tube while the V/III ratio was controlled by changing the flow of carrier gas. Growth of NWs was carried out for 3 h inside the furnace tube, and then these grown samples were allowed to cool down naturally. Under these conditions, NW growth occurred on Si(111) substrates by placing it in the temperature range of $450 \text{ }^\circ\text{C}$ – $550 \text{ }^\circ\text{C}$. We used argon as the carrier gas at a pressure of $<1 \text{ mTorr}$. This growth is advantageous as there is no by-product. There is no by-product produced during the growth process, which is quite significant for the growth of InSb NWs with high crystal quality as discussed. We observed a significant difference in the yield of NWs and in their morphology.

After the successful growth of NWs, all substrates were brought out from the furnace tube, and the crystallinity of the as-grown NWs are characterized using x-ray diffraction (XRD). Spectral response was investigated using Fourier transform infrared (FTIR) spectroscopy with the help of a Bruker Optics IFS 66V/S spectrometer. The surface and cross-sectional morphologies of NWs were characterized using a JEOL JSM 5800LV field emission scanning electron microscope (FESEM). The chemical composition of NWs was analyzed with energy dispersive x-ray spectroscopy (EDS), high-resolution transmission electron microscopy (HRTEM), and fast Fourier transform (FFT). Furthermore, we

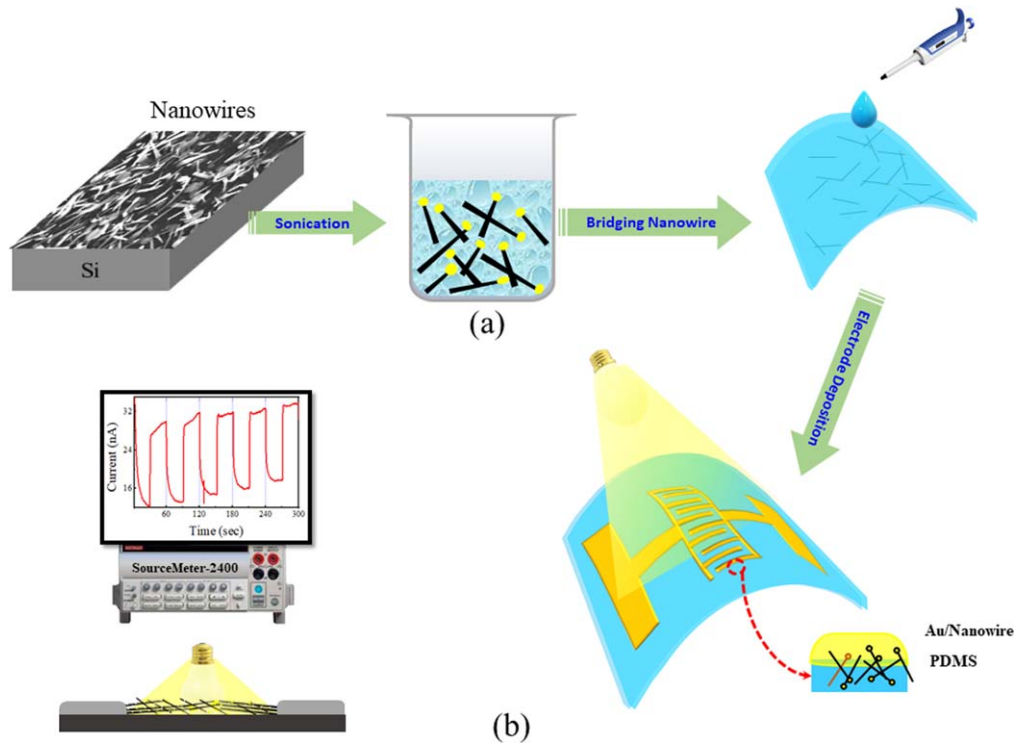


Figure 1. (a) Schematic of device fabrication by a conventional microfabrication technique. NWs grown in an alumina tube furnace, mixed in alcohol, and poured on PDMS substrate with Au electrode using a micropipette. (b) Device performance was then measured by using the Infrared photodetection setup.

have fabricated a wearable infrared photodetector by a facile prototype microfabrication technique.

The device fabricated from InSb NWs through the microfabrication route is shown in figures 1(a), (b). The flexible device was fabricated in a sequence which comprised the dispersion of InSb NWs from Si(111) substrate in alcohol followed by sonication for a few min. Afterward, the fabricated NWs were drop-casted on the PDMS substrate. After that, drying was done, followed by deposition of Au contacts. As a result, numerous NWs were interconnected in the form of a nano-bridge. The dimension of the device is $3 \times 3 \text{ cm}^2$, and that of the deposited electrodes is $1 \times 2.5 \text{ cm}^2$. This process is known as the so-called bridging of NW conventionality. To evaluate the infrared photodetectors, mid-infrared light of wavelength 5882 nm was used as an excitation light source with a 300 W xenon lamp. The transport and photosensitivity properties were analyzed using a semiconductor characterization system (4200-SCS, Keithley) at room temperature.

3. Results and discussion

A uniform Au thin film was deposited by annealing on Si substrates, with seeds forming nano-islands. The surface morphologies of these annealed substrates have been studied using FESEM, and resultant micrographs are shown in figures 2(a), (b). The micrographs show clear island formations which are due to the following facts. Firstly, the annealing at higher temperature segregated these

nanoparticles into small islands later used as seed catalysts for the growth of NWs. Secondly, with increasing temperature, the kinetic energy, and the mobility of Au atoms, also increase, which converts the thin film into nano-islands. Figure 2(f) shows the particle size distributions using Image J analysis software. It is observed that the annealing temperatures may alter the special distribution of the Au island with an average diameter of 110 nm.

FESEM images (figures 2(c), (d)) show uniform morphologies of the InSb NWs where the lengths of the NWs vary from 300 nm to $1 \mu\text{m}$ with a diameter of 10 nm to 120 nm depending on growth parameters. The presence of Au nanoparticles at the tip of the NWs confirm the VLS growth mechanism. A few NWs with a diameter of 30 nm were also observed, and these are known as quantum wires according to the definition of the Bohr radius. Spike-like NW morphologies suggest that the growth parameters may remarkably affect the dimension of the NWs. As reported previously, the growth mechanism of InSb and other III-Sb NWs starts from a crystal base. Figure 2(d) shows the InSb NWs grown on Si(111) at a relatively low pressure, i.e. 130 ml min^{-1} of carrier gas for which the growth is slower, while keeping the source and substrate in three different growth zones. The variations in carrier gas pressure control the diameter of the NWs grown, and the average NW lengths vary from $3 \mu\text{m}$ to $5 \mu\text{m}$. The density of NWs, as observed in the image, is consistent with that of the cross-sectional image. It is noted that higher growth rate strongly depends upon the growth temperature of the source and substrates; higher yield is

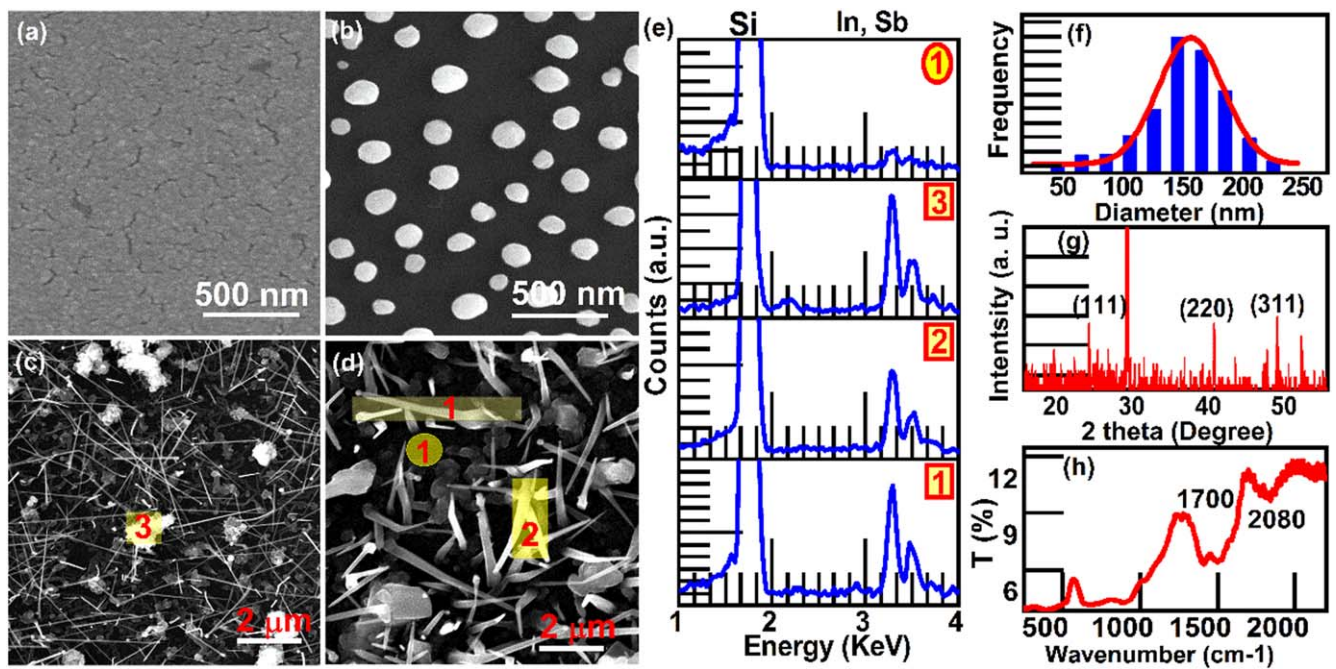


Figure 2. (a) FESEM images of the Au sputtered film, and (b) formation of nano-islands after calcination at high temperatures. The scale bar is 500 nm. (c), (d) Growth of NWs in the alumina tube furnace under various growth conditions. The scale bar is 2 μm . (e) The EDS analyses of the grown InSb NWs. The yellow rectangles on the NWs represent the areas where EDS is measured. The points 1, 2, 3 indicate the location of compositional measurements. The encircled area represents the location for background measurement. (f) Histogram for the island mapping using Image J, (g) XRD results of the InSb NWs obtained at different growth conditions, and (h) FTIR spectrum of the NWs.

obtained at a temperature of 550 $^{\circ}\text{C}$ while keeping carrier flow at 25 ml min^{-1} .

All XRD peaks represent pure zinc-blende InSb phase without secondary peaks from impurity materials or from precursors shown in figure 2(g). The crystallographic orientations at $2\theta = 23.76^{\circ}$, 39.31° , and 48.11° are attributed to the (111), (220), and (311) lattice planes with the zinc-blende recognized as the leading phase, while the peak at 28.44° originates from the substrate. Remarkably, depending upon the temperature, the grown NWs illustrate a single-crystalline nature along the entire length of the NW form, without any twin defects, visible dislocations, or stacking faults, etc. The growth direction of these NWs was along (111) further confirmed from the interplanar spacing value by the equation $d_{hkl} = \frac{a}{\sqrt{h^2 + k^2 + l^2}}$. The lattice parameters determined from XRD patterns were 0.37 nm and 0.23 nm, corresponding to the (111) and (220) planes (JCPDS-PDF card number 00-006-0208, cubic, cell constant, $a = 6.478 \text{ \AA}$, and space group F43m). In view of this, the variation of the peaks' intensity from the standard Powder Diffraction File database might be attributed to the orientation of NWs on the planar substrate which is under investigation. Recently, such a type of crystal growth under nanoscale confinement and nucleation has been reported [28].

EDS investigations were carried out for single NWs, nanostructures, and the substrate, and different regions are encompassed as shown in figure 2(e). The distribution of Sb and In on the NW structures reveals that the constituents are segregated uniformly. This analysis shows that both Sb and In are present with an equal percentage which confirms that

these NWs are purely InSb. It is observed that Au exists on the tip of the NW, in which case the ratios differ slightly, with the measured concentrations being In 50%, Sb 40.4%, and Au 9.9%, exhibiting a relatively smaller contribution of Sb, i.e. only slightly deviated from equiatomic constituents as deduced from crystallographic studies. The presence of Au nanoparticles at the tip of NWs confirms the VLS growth mechanism. The yellow encircled area shows the pure Si peak in the compositional spectrum. The optical transmission of the grown InSb NWs was measured using an FTIR spectrometer. This shows distinct absorption in the mid-infrared region, as shown in figure 2(h). The common absorption peaks of InSb NWs are at 1200 cm^{-1} ($\sim 8.3 \text{ mm}$), and 1650 cm^{-1} ($\sim 6.0 \text{ mm}$), which can be tuned by varying the ratios of constituents [29].

HRTEM imaging shown in figures 3(a)–(f) discloses the thoroughly faceted anatomy of the NWs, composed of zinc-blende phase with symmetry of single-crystalline domains, although there is a deficiency of Sb of 0.4% as depicted by XRD analysis. Crystallite size corresponds to the width of the diffraction peaks, which is around 5 nm. This shows that these NWs are highly faceted, and can exist together due to the similar domain size of either Sb-rich or stoichiometric structures.

FFT established a relationship between structure and diffraction pattern, herein the [20] (110) growth direction of the NW with fringes perpendicular to the NW axis. Straight-line dots in the FFT pattern of these NWs (figures 3(c)–(f)) confirm the single-crystalline nature of the NWs. Commonly, a crystal of InSb exists in the zinc-blende phase with a lattice constant of 6.48 \AA [30]. Lattice spacing measured using

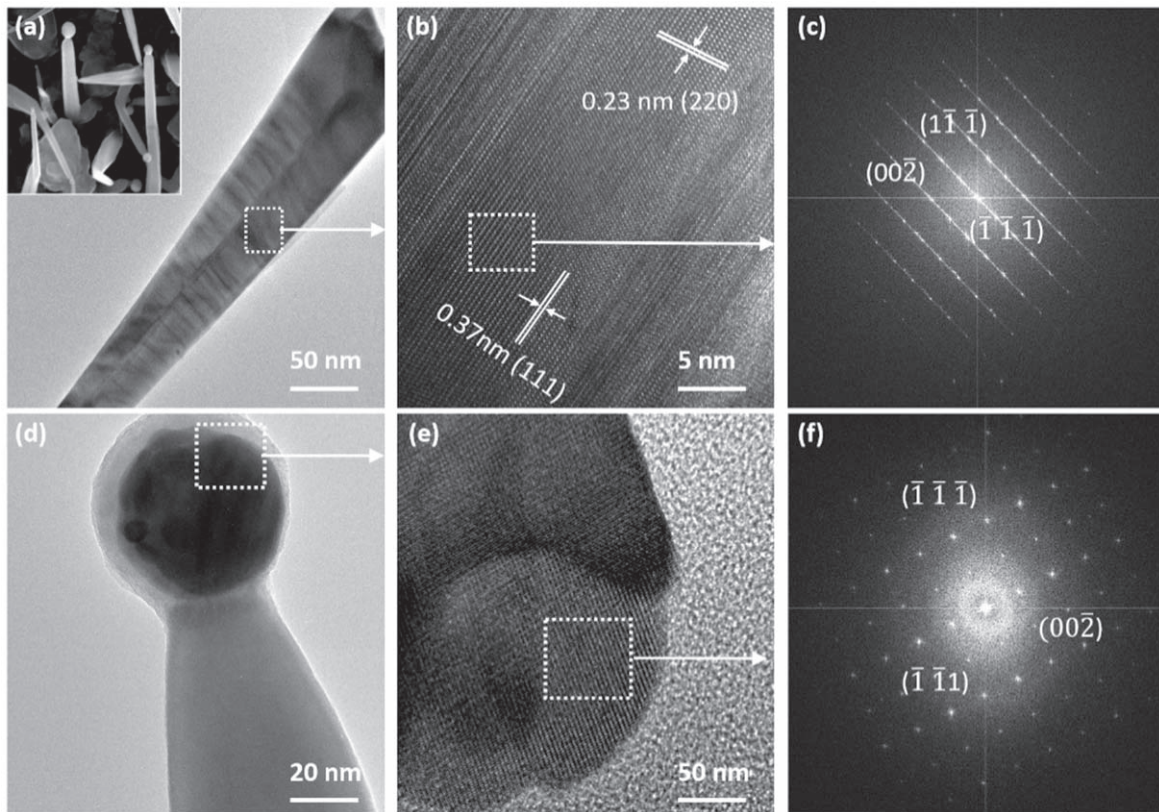


Figure 3. (a) Low-resolution TEM image of a single NW removed from the substrate and dissolved in alcohol (inset shows an FESEM image of the same morphology). (b) HRTEM image of the grown NWs with marked d -spacing. This magnified view of the parallel lattice planes of zinc-blende InSb NW indicates parallel lattice planes in the (111) and (220) directions. (c) FFT pattern of the same NWs in the identified crystallographic orientation. (d) NW loaded with Au catalyst at the end, (e) HRTEM of the Au seed particles, and (f) the corresponding FFT pattern.

HRTEM is also the same, confirming the zinc-blende structure of InSb NWs. An amorphous sheath covering the InSb NWs shown in the HRTEM image is an indication of the oxidation process most likely due to the formation of In_2O_3 as this is consistent with the diffraction pattern. Thus, electron diffraction or FFT of InSb NWs exhibits InSb zinc-blende crystal structure, i.e. the two major lattice spacings (also known as the interarticular distance) measured from XRD to be about 0.37 nm and 0.23 nm correspond to the (111) and (220) directions, respectively, of zinc-blende InSb.

For photodetector measurements, the grown NWs were dissolved in ethanol and then dispersed on flexible PDMS substrate before being dried and deposited with Au electrode. The fabricated device, as shown in figure 4(a), was placed in front of the xenon lamp to study the photodetection properties at different biased voltages. J - V (Current density - bias voltage) characteristics were measured for the InSb NWs under both illumination and dark conditions at 300 K, as shown in figure 4(a). The improved performance of the device based on InSb NWs is attributed to the high crystalline quality of the NWs. Both dark and light current curves show a linear dependence of the bias voltage, which indicates the formation of good ohmic contacts. The time dependent response of the fabricated device under white light and then infrared light is shown in figures 4(b), (c). In order to investigate the stability of the device based on InSb NWs, on/off photoresponse

(infrared and white light) photocurrents are measured with bias voltages of 0.1 V, 0.2 V, and 1 V at room temperature. Each cycle of photocurrent measurement comprises an interval of 30 s in which quick rise and fall of the current is observed (figure 4(b)). As the applied voltage increases, the photocurrent also increases; luckily there is no noticeable distortion during on/off, which indicates the excellent stability of the photodetector. There is a very short time lag of less than 1 s to achieve a steady-state. This time lag is associated with the alignment of ionic phases along the electric field. Here, a sequence in I - t (Current - time) measurements shows fast switching aspects of the device. The photocurrent and the dark current show approximately the same values for each cycle, and it takes about 60 s for one complete cycle. All these characteristics of the device based on InSb NWs show excellent long-term stability at room temperature.

These properties combined with a high on/off ratio and power-law dependence over a wide range of voltage or photosensitivity of more than 10^7 . All these properties make this device a promising candidate for fast optical switching and light detecting applications. Optical switches require such devices that show a very high on/off ratio toward current/voltage changes. This depicts recombination dynamics of photoexcited species in both photo and mid-infrared measurements. The fast components are related to the different recombination mechanisms on the surface of single-crystal

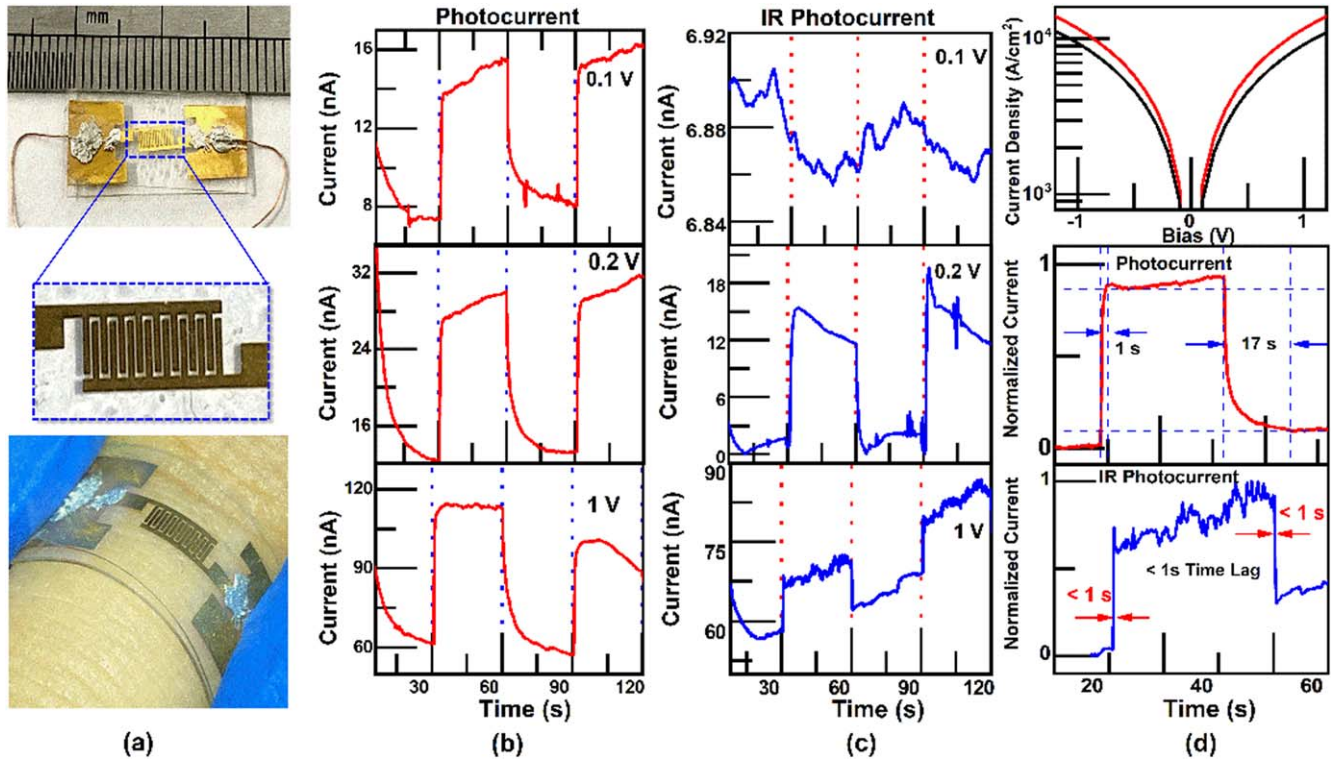


Figure 4. (a) Upper panel shows the flexible device with Au electrodes. Lower panel shows the device taped on the skin. Comparison of photodetector response of the fabricated device under (b) direct illumination of lamp and (c) near-infrared light. (d) J - V characteristics measured for InSb NWs under both illumination and dark conditions at 300 K (where red represents light while black shows dark), and high-resolution transient photoresponse of the device to illustrate the rise time and decay time constants.

Table 1. Calculated parameters for fabricated flexible infrared photodetectors based on InSb NWs.

Devices	λ (μm)	R_λ (A W^{-1})	EQE (%)	D^* (Jones)	NEP ($\text{W Hz}^{-1/2}$)	Ref.
InSb nanosheets	4.3	14.9	4.3×10^2	5.2×10^7	—	[33]
Single InSb NW	5.5	8.4×10^4	1.96×10^2	—	—	[34]
InGaSb NWs	1.5	6.0×10^4	4.8×10^6	3.0×10^9	—	[35]
InSb NW arrays	5.88	7.6×10^4	1.6×10^5	1.4×10^{12}	2.15×10^{-12}	This work

NWs that exhibit significantly improved average carrier lifetime. Thin films have drawbacks of flexibility so we introduce NWs on a flexible substrate.

The responsivity (R_λ), which is the generated photocurrent per unit power upon incident light on the effective area of the detector, can be calculated using the following equation [31, 32] $R_\lambda = (I_{\text{light}} - I_{\text{dark}})/(P \cdot A)$, where P is the illumination power density, A is the effective area of the illumination, and I_{light} (I_{dark}) are the photocurrent under light (dark). From the J - V graph in figure 4(d), we can deduce that current density $j_{\text{dark}} = 9320.3 \times 10^4 \text{ A m}^{-2}$ and $j_{\text{light}} = 11591.09 \times 10^4 \text{ A m}^{-2}$, while area A is $9 \times 10^{-4} \text{ m}^2$. The light power density was set to $P = 300 \text{ W m}^{-2}$.

The external quantum efficiency (EQE) is described as the number of electrons detected per incident photon and is calculated using the relation $EQE = hcR_\lambda/q\lambda$, where h is Planck's constant, c is the velocity of light, q is the electron charge and λ is the wavelength of the light source used for excitation. Calculated EQE for specific wavelength λ as

shown in the FTIR spectrum in figure 2(h) corresponds to 1700 cm^{-1} (5882 nm).

The detectivity (D) of the photodetector is calculated using the equation $D = R_\lambda/\sqrt{2qI_{\text{dark}}}$. The specific detectivity (D^*) is given by the equation $D^* = D\sqrt{A\Delta f}$, giving detectivity D for a 1 Hz bandwidth and a 9 cm^2 device area. The noise equivalent power (NEP) is given by the equation $NEP = \sqrt{A\Delta f}/D^*$, where A is the effective area (9 cm^2) and $\Delta f = 1 \text{ Hz}$.

In table 1, we compare our fabricated device based on InSb NW arrays with other low-dimensional materials. The calculated R_λ , EQE , D^* , and NEP are presented. In this case, with a xenon lamp of 300W and $V_{ds} = 1 \text{ V}$, the values of R_λ , EQE , and D^* are determined to be 76000 A W^{-1} , $1.6 \times 10^5\%$, and 1.4×10^{12} Jones, respectively. These measured performance parameters are already comparable to those of the state-of-the-art III-V NW photodetectors as shown in table 1. Our device showed significant response and extreme detectivity under illumination at room temperature.

It is clear from figures 4(b), (c) that the measured rise time for the fabricated device is less than 1 s while the current varies from 16 nA to 1 μ A. The resolution limit of the device is defined by the time during which the current becomes stable. Dark current shows a relatively slow response, because of the few surface charges that are still present to conduct the electricity even though the light is off. These components of dark current are reduced from 1 μ A to 8 nA within 2 s. It is speculated that the decaying of dark current is caused by migration of trap-released charge carriers. The time resolution of the prototype fabricated device depends on the light/dark current which is measured with an interval of 30 s. However, changes in the current vary up to several orders of magnitude, which may decrease the resolution from <1 s to 2 s. The origin of the observed fluctuations is possible due to the absorption/desorption of surface molecules. The photocurrent values reveal that no pumping or priming effects need to be taken into account for the explored timescale. Figure 4(d) shows the J - V characteristics measured for InSb NWs under both illumination and dark conditions at 300 K, and the high-resolution transient photoresponse of the device to illustrate the rise time and decay time constants for both photocurrent and infrared current. Here, the rise and decay time constants can be identified as less than 1 s. This efficient response up to the microsecond range represents better responses than many NW photodetectors reported in the literature. This fast response of the NW-based device can be attributed to homogenous NW composition and crystallinity, and appropriate controllable bandgap as well as enhanced surface-to-volume ratio of the one-dimensional NW channel.

4. Conclusions

In this work, flexible infrared photodetectors have been fabricated using high-quality InSb NWs, which exhibit a broad spectral detection range. Single-crystalline straight InSb NWs with zinc-blende crystal structure were produced using a VLS growth mechanism in a furnace tube with Au as seed particles. The structural characteristics were investigated using XRD, TEM, FESEM, and EDS, which confirmed the crystal structure of the InSb NWs. The diameter of grown InSb NWs varies from less than 10 nm to 150 nm. Moreover, our fabricated sensor demonstrated superior photoconductive sensitivity. To further enhance the performance of the photodetector, another layer of PDMS was deposited in order to passivate it from ambient environments, consequently creating a formidably sensitive detector. Such a flexible photodetector yields efficient rise and decay times down to 1 s, and short time lag for infrared detection. Based on dark current, the calculated specific detectivity of the flexible photodetector was 1.4×10^{12} Jones. This work illustrates the optoelectronic features of InSb NWs making them suitable for use in next-generation wearable devices. We envisage that these detectors will find many important applications in future.

Acknowledgments

We acknowledge support from the National Key R&D Program of China (Grant No. 2017YFA0206202), the Strategic Priority Research Program of the Chinese Academy of Sciences (Grant No. XDB30000000), the National Natural Science Foundation of China (Grant Nos. 12074302, 11704303), and the support of UAE University through the grant UPAR 12S013. We thank the Instrument Analysis Center of Xi'an Jiaotong University for their assistance with FESEM, TEM and XRD analysis.

Data availability statement

The data that support the findings of this study are available upon reasonable request from the authors.

ORCID iDs

Muhammad Shafa  <https://orcid.org/0000-0002-4462-0151>
Yi Pan  <https://orcid.org/0000-0003-1978-475X>

References

- [1] Zhang S *et al* 2020 Highly sensitive InSb nanosheets infrared photodetector passivated by ferroelectric polymer *Adv. Funct. Mater.* **30** 2006156
- [2] Elsayed M Y, Ismail Y and Swillam M A 2017 Semiconductor plasmonic gas sensor using on-chip infrared spectroscopy *Appl. Phys. A* **123** 113
- [3] Paul R K, Badhulika S and Mulchandani A 2011 Room temperature detection of NO₂ using InSb nanowire *Appl. Phys. Lett.* **99** 033103
- [4] Luo H and Cheng Y 2020 Thermally tunable terahertz metasurface absorber based on all dielectric indium antimonide resonator structure *Opt. Mater.* **102** 109801
- [5] Yang X, Wang G, Slattery P, Zhang J Z and Li Y 2010 Ultrasmall single-crystal indium antimonide nanowires *Cryst. Growth Des.* **10** 2479–82
- [6] Tomioka K, Yoshimura M and Fukui T 2012 A III–V nanowire channel on silicon for high-performance vertical transistors *Nature* **488** 189–92
- [7] Ghosh S *et al* 2020 Enhanced thermoelectric performance in the Ba_{0.3}Co₄Sb₁₂/InSb nanocomposite originating from the minimum possible lattice thermal conductivity *ACS Appl. Mater. Interfaces* **12** 48729–40
- [8] Davis M 2011 Indium antimonide large-format detector arrays *Opt. Eng.* **50** 061016
- [9] Shimatani M, Fukushima S, Okuda S and Ogawa S 2020 High-performance graphene/InSb heterojunction photodetectors for high-resolution mid-infrared image sensors *Appl. Phys. Lett.* **117** 173102
- [10] Burleigh D, Siikanen S, Miikkulainen P, Kaarre M, Juuti M and Stockton G R 2012 *In-line particle measurement in a recovery boiler using high-speed infrared imaging* Proc. SPIE **8354** 83540M
- [11] Thomas P J, Hollinger A B and Wiens R H 1993 Adaptive infrared forest-fire sensor *Infrared Imaging Systems: Design, Analysis, Modeling, and Testing IV* ed G C Holst 1969

- (Orlando, FL: SPIE) 370–81 International Society for Optics and Photonics
- [12] Wang P *et al* 2020 The evolution of flexible electronics: from nature, beyond nature, and to nature *Adv. Sci.* **7** 2001116
- [13] Qiao Y *et al* 2018 Multilayer graphene epidermal electronic skin *ACS Nano* **12** 8839–46
- [14] Lee G-H *et al* 2020 Multifunctional materials for implantable and wearable photonic healthcare devices *Nat. Rev. Mater.* **5** 149–65
- [15] Park H L, Lee Y, Kim N, Seo D G, Go G T and Lee T W 2020 Flexible neuromorphic electronics for computing, soft robotics, and neuroprosthetics *Adv. Mater.* **32** e1903558
- [16] Chen C Y *et al* 2012 Probing surface band bending of surface-engineered metal oxide nanowires *ACS Nano* **6** 9366–72
- [17] Zhai T, Li L, Wang X, Fang X, Bando Y and Golberg D 2010 Recent developments in one-dimensional inorganic nanostructures for photodetectors *Adv. Funct. Mater.* **20** 4233–48
- [18] Wu P *et al* 2011 Impurity-dependent photoresponse properties in single CdSe nanobelt photodetectors *ACS Appl. Mater. Interfaces* **3** 1859–64
- [19] Lee K-H, Lee J-W, Park H-D, Jeung W-Y and Lee J-Y 2005 Electrochemical formation and characterization of III–V compound semiconductor InSb nanowires *J. Korean Electrochem. Soc.* **8** 130–4
- [20] Park H D, Prokes S M, Twigg M E, Ding Y and Wang Z L 2007 Growth of high quality, epitaxial InSb nanowires *J. Cryst. Growth* **304** 399–401
- [21] Badawy G *et al* 2019 High mobility stemless InSb nanowires *Nano Lett.* **19** 3575–82
- [22] Yang Y, Li L, Huang X, Li G and Zhang L 2007 Fabrication and optical property of single-crystalline InSb nanowire arrays *J. Mater. Sci.* **42** 2753–7
- [23] Jin Y J *et al* 2020 Hetero-epitaxial growth and mechanism of one-dimensional InSb nanostructures on GaAs substrate by MOCVD *J. Alloys Compd.* **823** 153758
- [24] Chandrashekhara P, Sreeram V, Jeong H K, Jacek J, Zhiqiang C and Mahendra K S 2010 Self-nucleation and growth of group III-antimonide nanowires *Semicond. Sci. Technol.* **25** 024014
- [25] Ye Q L, Yamada T, Liu H, Scheffler R, Mingo N and Leverenz R 2006 Single crystal InSb nanowires: synthesis, characterization, properties and applications *MRS Online Proceedings Library* **940** 705
- [26] Singh A P, Roccapiore K, Algarni Z, Salloom R, Golden T D and Philipose U 2019 Structure and electronic properties of InSb nanowires grown in flexible polycarbonate membranes *Nanomaterials*. **9** 1260
- [27] Chen H, Sun X, Lai K W C, Meyyappan M and Xi N 2009 Infrared detection using an InSb nanowire *IEEE Nanotechnology Materials and Devices Conference (Traverse City, MI, USA, 2-5 June 2009)* (IEEE) **212**–6
- [28] Jin Y J, Zhang D H, Liu H F and Tang X H 2016 Self-nucleation growth of InSb nanowires based on indium droplets under the assistance of Au nano-particles by MOCVD *Mater. Lett.* **185** 77–80
- [29] Shafa M *et al* 2016 Mid-infrared photodetectors based on InSb micro/nanostructures grown on low-cost mica substrates *Mater. Lett.* **169** 77–81
- [30] Maurice A, Haro M L, Hyot B and Reiss P 2013 Synthesis of colloidal indium antimonide nanocrystals using stibine *Part. Part. Syst. Charact.* **30** 828–31
- [31] Liu Y, Sun J, Yang Z, Yang D, Ren X, Xu X, Yang Z and Liu S F 2016 20-mm-largesingle-crystalline formamidinium-perovskite wafer for mass production of integrated photodetectors *Adv. Opt. Mater.* **4** 1829–1837
- [32] Ueda T, An Z, Hirakawa K and Komiyama S 2008 Charge-sensitive infrared phototransistors: characterization by an all-cryogenic spectrometer *J. Appl. Phys.* **103** 093109
- [33] Zhang S *et al* 2020 Highly sensitive InSb nanosheets infrared photodetector passivated by ferroelectric polymer *Adv. Funct. Mater.* **30** 2006156
- [34] Kuo C H, Wu J M, Lin S J and Chang W C 2013 High sensitivity of middle-wavelength infrared photodetectors based on an individual InSb nanowire *Nanoscale Res. Lett.* **8** 327
- [35] Li D *et al* 2019 Ultra-fast photodetectors based on high-mobility indium gallium antimonide nanowires *Nat. Commun.* **10** 1664